# Nonlocal transport due to Langmuir circulation in a coastal ocean

T. Kukulka,[1] A. J. Plueddemann,[2] and P. P. Sullivan[3]

Received 6 July 2012; revised 1 October 2012; accepted 9 October 2012; published 11 December 2012.

[1] We present observations and simulations of large-scale velocity structures associated with turbulent boundary layer dynamics of a coastal ocean. Special purpose acoustic Doppler current profiler measurements revealed that such structures were frequently present, in spite of complex coastal environmental conditions. Large eddy simulation results are only consistent with these observations if the Langmuir circulation (LC) effect due to wave-current interaction is included in the model. Thus, model results indicate that the observed large-scale velocity structures are due to LC. Based on these simulations, we examine the shift of energetics and transport from a local regime for purely shear-driven turbulence to a nonlocal regime for turbulence with LC due to coherent large-scale motions that span the whole water column. Without LC, turbulent kinetic energy (TKE) dissipation rates approximately balance TKE shear production, consistent with solid wall boundary layer turbulence. This stands in contrast to the LC case for which the vertical TKE transport plays a dominant role in the TKE balance. Conditional averages argue that large-scale LC coherent velocity structures extract only a small fraction of energy from the wavefield but receive most of their energy input from the Eulerian shear. The analysis of scalar fields and Lagrangian particles demonstrates that the vertical transport is significantly enhanced with LC but that small-scale mixing may be reduced. In the presence of LC, vertical scalar fluxes may be up gradient, violating a common assumption in oceanic boundary layer turbulence parameterizations.

**Citation:** Kukulka, T., A. J. Plueddemann, and P. P. Sullivan (2012), Nonlocal transport due to Langmuir circulation in a coastal ocean, *J. Geophys. Res.*, *117*, C12007, doi:10.1029/2012JC008340.

## 1. Introduction

[2] Upper ocean turbulence determines the momentum, scalar, and material distributions in the mixed layer and greatly influences transport processes across the air-sea interface [*Leibovich*, 1983; *Melville*, 1996; *Thorpe*, 2004; *Wanninkhof et al.*, 2009; *Sullivan and McWilliams*, 2010]. Both breaking and nonbreaking ocean surface waves critically affect upper ocean turbulence. Breaking ocean surface waves transfer some of their energy to enhance oceanic near-surface turbulence intensities and dissipation rates, which contribute to near-surface mixing [*Craig and Banner*, 1994; *Melville*, 1996; *Terray et al.*, 1996]. Nonbreaking ocean surface waves influence upper ocean turbulence because the wave-induced residual circulation (Stokes drift) tilts vertical vorticity into the direction of wave propagation. As a consequence, wind-aligned roll vortices form, so-called Langmuir circulation (LC), that may strongly facilitate transport processes [*Leibovich*, 1983; *Thorpe*, 2004].

[3] Previously, upper ocean turbulence has been investigated in the wave breaking influenced surface layer in the upper 3 m of a 16 m deep coastal ocean offshore of Martha's Vineyard [*Gerbi et al.*, 2008, 2009]. The observed turbulent kinetic energy (TKE) dissipation rates are not balanced by local TKE production terms, so that the transport of TKE plays a key dynamical role in the ocean surface boundary layer, which is inconsistent with rigid wall boundary layer turbulence. The enhanced mixing has been attributed to turbulence generation by wave breaking and LC. Recent large eddy simulation (LES) results of these observed conditions support the interpretation that breaking waves significantly influence turbulence statistics and related mixing in the upper 3 m (M. Li et al., personal communication, 2011). An outstanding problem of understanding the observations is to identify the role of LCs in energetics and transport at middepth.

[4] Recent observations and simulations highlight the critical influence of LCs on turbulent mixing processes in a coastal, shallow ocean [*Gargett et al.*, 2004; *Gargett and Wells*, 2007; *Tejada-Martinez and Grosch*, 2007]. Many characteristics of coastal LCs are consistent with LCs in deep water, such as the three-dimensional velocity structure. Unlike in deep water, however, LC may fill the whole water column in a shallow ocean to effectively couple the surface and bottom boundary layers [*Gargett et al.*, 2004]. Near-bottom intensifying along-wind velocity jets are typically located below LC

[1]School of Marine Science and Policy, College of Earth, Ocean, and Environment, University of Delaware, Newark, Delaware, USA.
[2]Department of Physical Oceanography, Woods Hole Oceanographic Institution, Woods Hole, Massachusetts, USA.
[3]National Center for Atmospheric Research, Boulder, Colorado, USA.

Corresponding author: T. Kukulka, School of Marine Science and Policy, College of Earth, Ocean, and Environment, University of Delaware, 211 Robinson Hall, Newark, DE 19716, USA. (kukulka@udel.edu)


0148-0227/12/2012JC008340

downwelling regions, where they contribute to sediment resuspension. This jet was captured in the shallow water large eddy simulation (LES) model based on the Craik-Leibovich equations [*Tejada-Martinez and Grosch*, 2007]. These LES results reveal important differences between pure shear-driven flow and flow that also includes Stokes drift forcing to generate LC.

[5] Understanding LC in a coastal ocean is very complex, because wind and wave conditions are often highly variable, so that a range of wave ages, misaligned wind and wavefields, and "mixed" seas with swell are encountered [*Churchill et al.*, 2006]. Misaligned wind and wavefields result in weakened LC activity [e.g., *Gnanadesikan and Weller*, 1995]. Furthermore tidal currents generally influence LC dynamics. The tidally driven bottom boundary layer ejects fluid parcels, so-called boils, which travel upward to the surface boundary layer and disrupt LCs. Such disruptions have been observed in a 45 m deep unstratified ocean for strong tidal currents with speeds of up to 1 m/s [*Nimmo-Smith et al.*, 1999; *Thorpe*, 2000]. Another mechanism of the tidal influence is due to mean crosswind shear, which can distort and destroy LC cells in a coastal ocean [*Kukulka et al.*, 2011].

[6] The goal of the paper is to examine the transport and energetics of coastal ocean LCs, which are influenced by tides and nonequilibrium seas. In section 2 we discuss observations that indicate the frequent presence of LC in a coastal ocean, in spite of the complex coastal ocean conditions. In section 3 we present a LES model that captures features of typical LC observations. Finally, by investigating energy budgets, scalar transport, and particle statistics, based on simulations, we highlight the significance of LC in energetics and transport (section 4).

## 2. Observations

### 2.1. Methodology

[7] The basic methodological approach has been described by *Kukulka et al.* [2011] and is summarized here.

#### 2.1.1. CBLAST-Low Experiment

[8] The Coupled Boundary Layers and Air-Sea Transfer Experiment in Low Winds (CBLAST-low) was conducted on the west Atlantic continental shelf about 3 km south of Martha's Vineyard, Massachusetts, during 2001 and 2003, where the water depth $H$ was approximately $H = 16$ m [*Edson et al.*, 2007; *Gerbi et al.*, 2009]. The CLBAST-low data include observations of (1) two-dimensional ocean surface wavefields [*Churchill et al.*, 2006]; (2) heat and momentum air-sea fluxes; (3) vertical profiles of temperature, salinity, and currents; and (4) subsurface turbulence estimates from "fan beam LC detectors" [*Plueddemann et al.*, 2001].

[9] This fan beam instrument consists of special purpose acoustic Doppler current profiler (ADCP) that measures horizontal velocities of surface trapped bubbles [*Smith*, 1989; *Zedel and Farmer*, 1991]. In the presence of LC, sonar beams oriented perpendicular to the wind direction (crosswind) detect horizontal bands due to velocity convergence zones of coherent surface LC structures (Figure 1). The analysis presented here is based on the fan beam deployment from the end of September to beginning of November of 2003, when buoyancy effects were often negligible. Wind, wave, and current conditions were generally complex during this period with turning winds, nonequilibrium seas, and tides (Figure 2).

[10] Buoyancy surface forcing likely plays a secondary role in the turbulence dynamics during the analysis period, since the magnitude of the Monin-Obukhov length is usually much larger than the ocean depth.

[11] In general the observed stratification at the study site may be complex because of horizontal advection [see, e.g., *Lentz et al.*, 2010] and may at times influence LC dynamics. The following arguments suggest, however, that stratification is often weak, in the sense $H \ll L_O$, where the water depth $H$ is taken as a vertical LC length scale. A length scale for which buoyancy effects become important is estimated by $L_O = w_{LC}/N$, where $N = \sqrt{-g\rho_0^{-1}\Delta\rho/\Delta z}$ denotes a scale for the buoyancy frequency with reference density $\rho_0$ and gravitational acceleration $g$. The bulk density gradient $\Delta\rho/\Delta z$ is computed from salinity and temperature profile measurements, while the vertical LC velocity scale $w_{LC}$ is estimated based on scaling the continuity equation and from fan beam observations. This approach results in $w_{LC} \approx 2$ cm/s, which is in close agreement with LES results. In the presence of LC, we find that $H/L_O < 0.1$ for 62% of the times when stratification effects are likely dynamically insignificant. In a first attempt to model LC observations (below), we neglect buoyancy effects.

#### 2.1.2. Fan Beam Observations

[12] In order to compare measurements with model results, it is necessary to understand the spatial extent of the surface measurements. The near-surface bubble distribution decreases roughly exponentially in the vertical with a decay scale around 1.0 to 1.5 m and confines the vertical extent of the measurement volume to about 3 m, depending on wind and wave conditions [*Plueddemann et al.*, 2001]. Maximum horizontal range along the surface also varies with wind and wave conditions [*Plueddemann et al.*, 2001]. For this study, a conservative, fixed aperture of 85 m was used with "range cells" along the sea surface with dimensions of about 2.4 m along beam and 5 m cross beam. The limited aperture implies that spatial scales longer than 85 m are not resolved. The fan beam ping rate was 1 Hz, with 56-ping ensembles recorded every minute.

[13] Postprocessing was applied to average over surface wave orbital velocities [*Smith*, 1992] and to extract a robust signal of near-surface velocity convergence regions from the noisy acoustic measurements [see also *Gerbi et al.*, 2009]. Based on conservative quality control criteria, only data from two of the four beams (beam number two and three) were processed for ranges between 37 m and 123 m (bins 9 to 45). During the majority of the analysis period beams two and three were approximately directed toward SSW (210°) and west (270°), respectively (Figure 2, fourth panel). The instantaneous angle between the beams and LC convergence zones (assumed to be oriented between wind and wave directions) often exceeds 45° and is never below 30°, so that a significant fraction of surface convergence velocities are along beam. Each beam was processed separately to produce a velocity anomaly for 20 min time intervals. A temporal high-pass filter with a half-power point at 40 min was first applied to remove the tidal variability that dominated the raw velocities. The high-passed velocities were then detrended in time and range within contiguous 20 min processing windows. To capture only the largest scales, a moving average with a window length of 14 m was further applied. This final

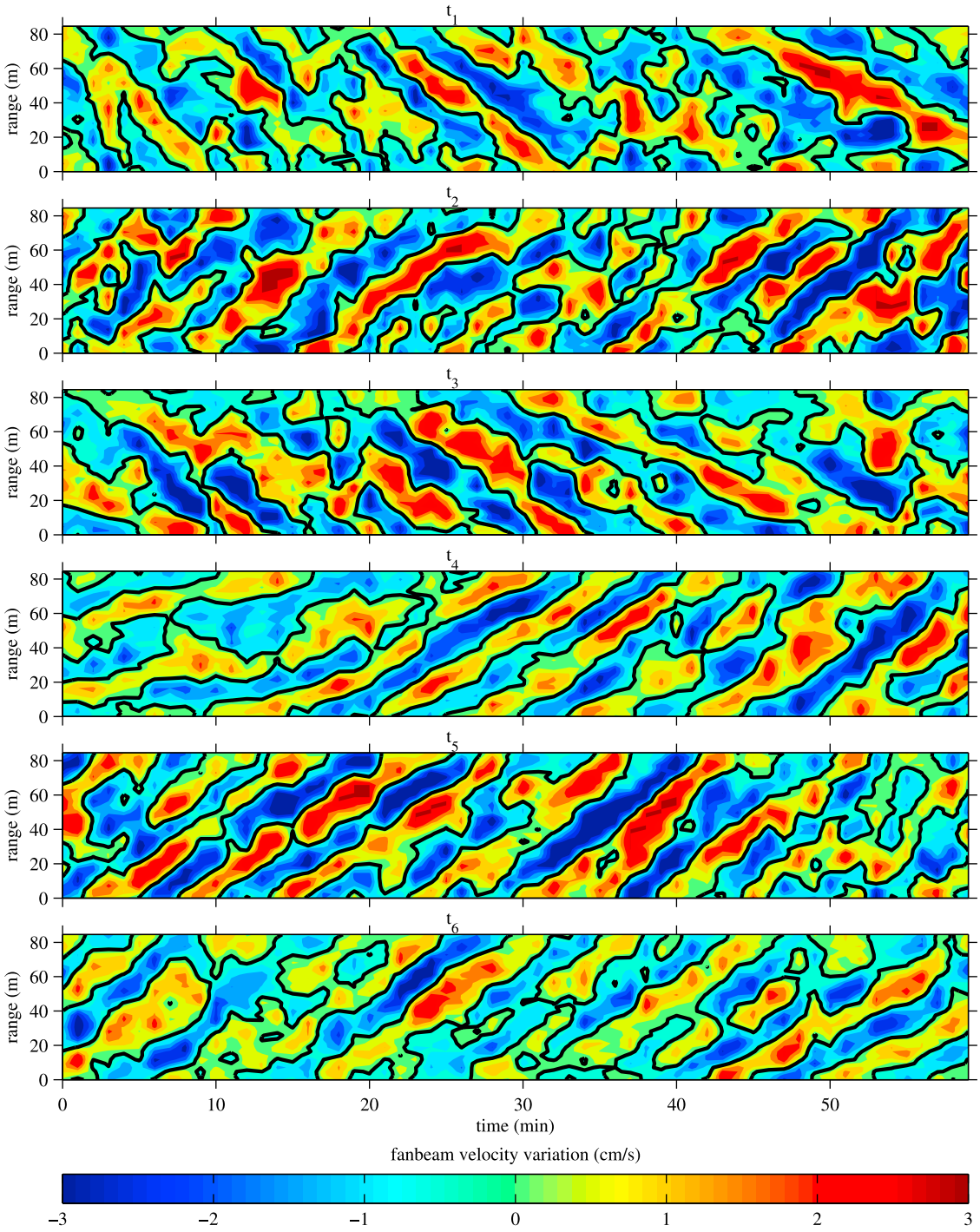


**Figure 1.** Fan beam crosswind velocity variations as function of time and fan beam range indicate the presence of LC through persistent crosswind convergence and divergence regions. Black lines are zero velocity convergence or divergence regions. The different times $t_i$ correspond to a range of wind and wave conditions (see Figure 2).

filtered velocity anomaly is denoted by $v'$. The root-mean-square of this quantity, based on 20 min contiguous intervals, denoted VRMS, was recorded for each beam.

[14] It is important to recognize that spatial features with horizontal scales smaller than, say, 2 times the water depth (32 m), can be attenuated significantly by the postprocessing described above. Thus, the fan beam velocity observations capture only relatively large spatial variations over scales from about 30 m to 85 m, which is in the expected range of well-developed LC [*Gargett and Wells*, 2007] and consistent with the simulations presented below (horizontal LC scales of about 6 $H$ = 96 m are still detectable, but attenuated). Measured surface velocity variations are likely underestimated due to the misalignment of convergence regions and fan beam

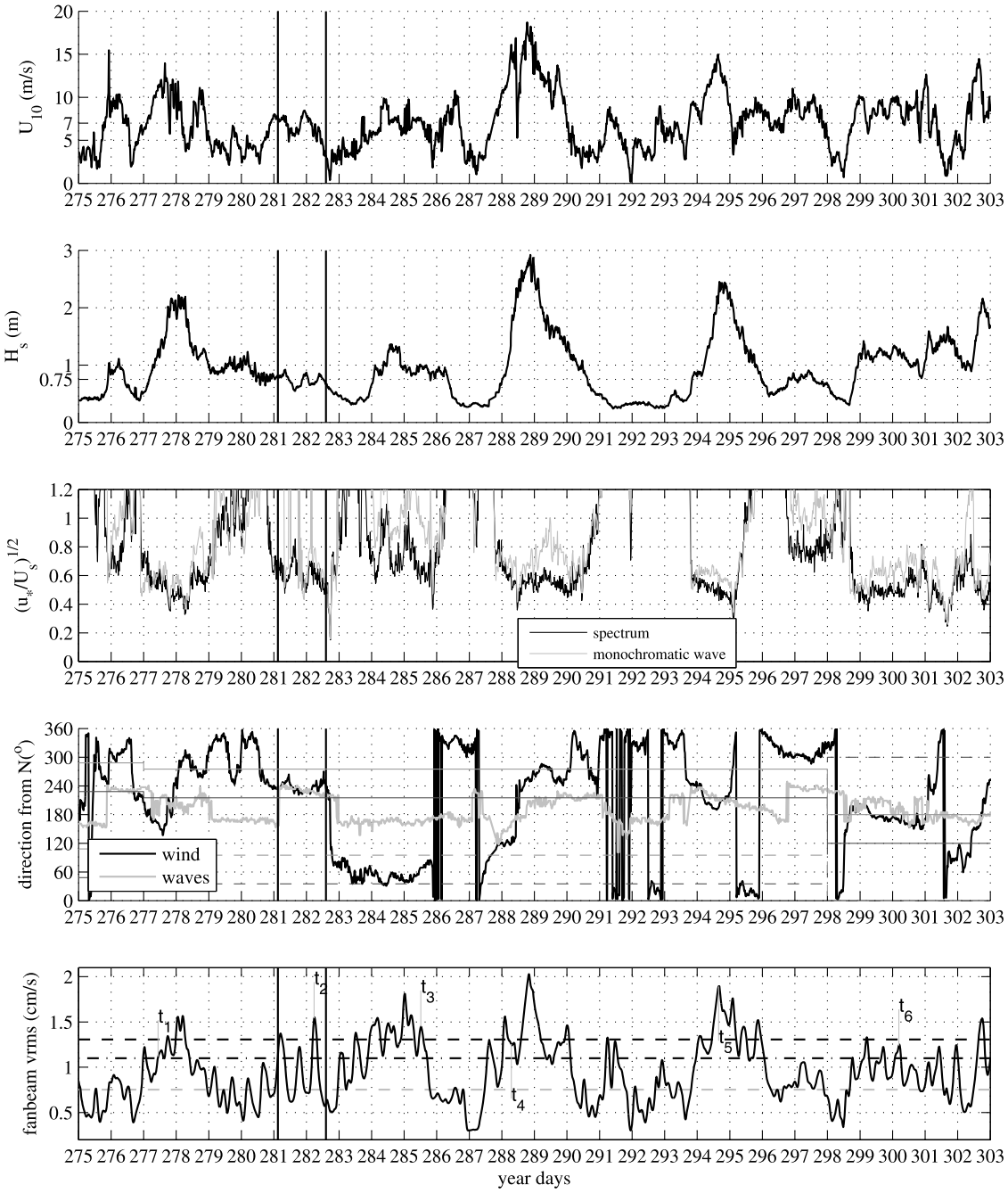


**Figure 2.** The presence of LC is strongly influenced by wind and wave conditions. Wind rows of strong crosswind convergence/divergence regions are often observed for VRMS ≥ 1.1 cm/s (dash-dotted line, compare with Figure 1). Wind and wave directions are aligned and approximately constant with $U_{10} \approx 7$ m/s and $H_s = 0.75$ m/s during the time interval marked by the two vertical lines. The simulated fan beam VRMS for these wind and wave conditions is significantly larger with (black dashed line) than without (gray dashed line) LC forcing. The fan beam look directions for beams two and three are shown as gray and black, respectively (±180° dashed lines).

look directions as well as due to the averaging, which depends on the mean advection speed, as discussed by *Kukulka et al.* [2011].

### 2.2. Results

[15] Relatively strong larger-scale surface velocity convergence and divergence regions are frequently present (Figure 1). Strong surface velocity convergence and divergence zones appear as organized bands, tilted due to slow cross-beam advection. Whenever the advection velocities change significantly, these bands curve in the time-range plots. The spacing between bands ranges from 40 m to 60 m, and both their spacing and width vary. Coherent subsurface velocity features often persist for 1 h or more.

[16] Organized fan beam velocity variations coincide with a relatively large fan beam VRMS (compare Figures 1 and 2). Typically, bands of strong subsurface convergence and divergence velocities occur for $VRMS > 1.1$ cm/s, while for $VRMS < 1.1$ cm/s fan beam velocity variations often appear less organized (examples are shown in Figure 6 of *Kukulka et al.* [2011]). Therefore, we designate a VRMS threshold of $VRMS = 1.1$ cm/s to define "the presence of LC" (all VRMS values above the dash-dotted line in Figure 2 (fifth panel)). Note that this threshold is specific to our study and that different VRMS thresholds have been introduced previously [e.g., *Plueddemann et al.*, 1996]. The simulations presented below support that enhanced fan beam VRMS, which only indicates the occurrence of larger spatial scale velocity variations, are indeed due to LC.

[17] As found in prior studies, LCs are relatively common, even for modest wind and wave forcing (Figure 2). Some fan beam VRMS variability is due to variations in wind and wave conditions. For example, during year day 293 to 295 VRMS increases as the wind speed and wave height become greater. However, for complex coastal ocean conditions LC strength is not simply related to wind speed and wave height. A tidal signature in the VRMS signal is apparent throughout (e.g., around year day 282) and may be caused by the obstructing influence of crosswind tidal shear on LC [*Kukulka et al.*, 2011]. Sufficiently large misalignment of wind and wavefields could prevent LC initiation, as evident around year day 276 when moderate wind speeds and significant wave heights would support LC generation, yet observed VRMS is small and the misalignment angle is large. Finally, ocean turbulence adjusts to the changing forcing wind and wavefields, so that LCs are likely not always in equilibrium with the external forcing.

[18] We next examine the wind and wave conditions that are particularly favorable or unfavorable for LC generation during the analysis period. The competition between shear and Langmuir instabilities is described by the turbulent Langmuir number $La_t = (u_*/u_{s0})^{1/2}$, where $u_*$ is the water friction velocity and $u_{s0}$ denotes the surface Stokes drift [*McWilliams et al.*, 1997]. *Li et al.* [2005] identified that for $La_t < 0.7$ and idealized open ocean conditions turbulence is dominantly driven by LC. Under more general conditions the shape of the Stokes drift profile, which is determined by the full waveheight spectrum, also influences Langmuir turbulence [e.g., *Harcourt and D'Asaro*, 2008]. For comparison with previous studies, we take two approaches to compute $La_t$. The first one is based on a monochromatic wave estimate, which is consistent with the observed significant wave height and peak wave period (gray line, Figure 2 (third panel)). For the second estimate we integrate the Stokes drift contributions from observed spectral wave components with a frequency cutoff at 0.4 Hz, which is consistent with the study of *Gerbi et al.* [2009] (black line, Figure 2 (third panel)). The latter exceeds the former estimate because it weighs more heavily short wave contributions. It also captures more accurately the average Stokes drift shear, which is critical in setting up the LC instability [*Leibovich*, 1977].

[19] Only 72% of events designated as LC by our criterion have $La_t < 0.7$ ($La_t$ is here based on the spectral estimate), which indicates that the idealized open ocean $La_t$ threshold differs from that applicable to a shallow ocean with complex wind and wave conditions. This is consistent with previous shallow ocean results for which $La_t > 0.7$ and turbulence is characterized by LC [*Gargett and Wells*, 2007; *Kukulka et al.*, 2011]. Note that LC may not be present in spite of a relatively small $La_t$ if the wind wave misalignment or tides cause unfavorable conditions for LC generation.

[20] In the presence of LC, the wind speeds exceed 5 m/s in 93% of the times and the significant wave heights are over 0.5 m in 93% of all times. That is, relatively high wind speeds and wave heights form a "near necessary condition" for LC presence. On the other hand, for $U_{10} < 5$ m/s and $H_s < 0.5$ m LCs are not present in 93% and 90% of all times, respectively. The smallest $H_s$ with LC presence range from 0.5 m to 1.0 m (e.g., from year day 281 to 282). Thus, relatively low wind speeds and wave heights provide a "near sufficient condition" for no LC presence. In the presence of LC, the median wind and wave conditions are $U_{10} \approx 8.3$ m/s and $H_s \approx 1.3$ m. As expected, these values exceed the median $U_{10} \approx 6.9$ m/s and median $H_s \approx 0.9$ m for the full analysis period. Based on these observations, we next constrain an LES model, which is used to investigate the significance of the frequently observed coastal LCs.

## 3. Coastal LES Model

### 3.1. Basic Approach

[21] The coastal ocean large eddy simulations (LES) are based on our previous model [*Kukulka et al.*, 2011]. In this approach, we have modified a laterally periodic large eddy simulation model for the open ocean [*McWilliams et al.*, 1997]. The open ocean model solves the CL equation spatially averaged over the subgrid scale (SGS). The CL momentum equations capture LC dynamics by a vortex force that involves the Stokes drift. Earth rotation (Coriolis force) is not included in our model, similar to the study by *Tejada-Martinez and Grosch* [2007]. Buoyancy effects are also not included. A solid wall bottom boundary condition has been implemented based on the atmospheric approach from *Sullivan et al.* [1994]. Turbulent SGS fluxes are parameterized via an SGS eddy viscosity that depends on the SGS turbulent kinetic energy (TKE). The SGS TKE, in turn, is determined from a prognostic equation [*Deardorff*, 1973]. Closer to the boundaries the SGS model is modified for better correspondence with Monin-Obukhov similarity theory [*Sullivan et al.*, 1994]. For distances more than 1 m away from the boundaries, the simulations resolve over 90% of the flux and energy carrying eddies, so that the LES results presented here are well resolved and depend only weakly on the details of the SGS parameterization [*Pope*, 2008]. Sensitivity studies indicate that our domain and grid resolution are appropriate and not sensitive to the subgrid scale closure scheme and hydrodynamical roughness length (T. Kukulka et al., A large eddy simulation sensitivity study of coastal Langmuir circulations, manuscript in preparation, 2012).

[22] The bottom stress is parameterized by a drag coefficient, which has been determined based on a best fit for direct covariance measurements of Reynolds stresses at $z = 0.75$ m above bottom, where $c_D = 0.0034$ (J. Trowbridge, personal communication, 2011). During the measurement period, stress and dissipation estimates were roughly consistent with a constant-stress logarithmic layer, so that $c_D$ can be expressed in terms of a roughness length of $z_0 = 0.75\ \text{m} \times \exp(-\kappa/\sqrt{c_D}) \approx 0.001$ m ($\kappa = 0.4$ is the von Karman

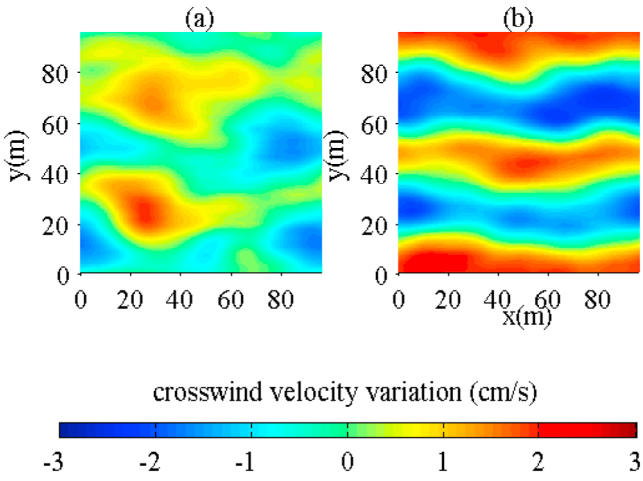


**Figure 3.** LES solution of $v'$ for $U_{10} = 7$ m/s at $z = -1.2$ m (a) without and (b) with LC forcing. An averaging procedure similar to the ones of the observational data processing has been applied (60 s time and spatial averaging). Note same color range as in Figure 1.

constant). Consistent with the Reynolds stress measurements from the study site, we employ a roughness length of $z_0 = 0.001$ m in our LES model to relate the local near bottom velocities to local bottom stresses.

[23] The total ocean depth is set to $H = 16$ m consistent with CBLAST-low observations with 100 vertical grid points. The horizontal domain is 96 m × 96 m with 256 × 256 grid points.

[24] For all LES runs the Stokes drift was imposed based on a monochromatic surface wave with a significant wave height and frequency (wavelength) consistent with observations. The dispersion relation with depth effects was used to calculate the Stokes drift. The wavelength $\lambda$ was kept fixed at 40 m, which corresponds roughly to 5 s wave periods. Generally, the Stokes drift decay with depth (related to $\lambda$) plays a significant dynamical role [*Polton and Belcher*, 2007; *Harcourt and D'Asaro*, 2008], but is not further investigated in this study as $\lambda = 40$ m represents a typical value for the wind-driven part of the observed wave spectrum [*Churchill et al.*, 2006].

[25] It is useful to compare the LES approach taken by *Tejada-Martinez and Grosch* [2007] and that taken in this study. One general challenge in LES is to capture small-scale turbulence close to walls. Two approaches are common [e.g., *Pope*, 2008]: (1) to resolve near wall motion, the approach taken by *Tejada-Martinez and Grosch* [2007], and (2) to model near wall motion, the approach taken by our group. Resolving near-wall motion has the advantage that fewer assumptions are necessary, but the disadvantage that the computational cost increases with Reynolds number ($Re$). Such $Re$ limitations do not apply when the boundary layer flow is modeled; however, there may be uncertainty in the applicability of the near-wall turbulence model. For example, *Tejada-Martinez et al.* [2012] found that the log layer near the bottom boundary is disrupted by LC and could affect the interior flow. Their study, however, also indicates that for the parameters of our LES ($La_t \sim 0.7$, $\lambda = 2.5\ H$) disruption is unlikely to be significant.

### 3.2. Comparison With Observations

[26] The goal of the simulation is to contrast coastal ocean turbulence dynamics with and without LC effects. In order to accomplish this, it is not necessary to model realistically every aspect of the evolving observed complex wind, wave, and tide conditions. Instead, as a first step, we focus on a single event during year days 281 and 282.5, when the LES/observation comparison is relatively straightforward. During this event wind and wave directions are nearly aligned and wind speed and wave height are approximately constant with $U_{10} \approx 7$ m/s and $H_s = 0.75$ m (Figure 2). These values are also close to the median observed $U_{10}$ and $H_s$ for the full analysis period.

[27] During year days 281 and 282.5 the fan beam VRMS frequently exceeds 1.1 cm/s, indicating the presence of LC (see above), but oscillates with a period of about 12 h. Previously, we attributed this tidal modulation to LC obstruction when tidal shear is strong and the VRMS low (compare with Event 1 of *Kukulka et al.* [2011]). In this paper, we focus on the observed large-scale velocity features with enhanced VRMS that we attribute to LC.

[28] Applying a similar averaging procedure as for the fan beam observations [see also *Kukulka et al.*, 2011], the simulated fan beam VRMS agrees significantly better with the observations if the LC effect is included in the model (Figures 2 and 3). Without LC, the model yields VRMS = 0.75 cm/s at $z = -1.2$ m (gray dashed line in Figure 2), while with LC *VRMS* is significantly larger with VRMS = 1.31 cm/s (black dashed line in Figure 2). Note the presence of weak divergence/convergence regions in the flow without LC due to "Couette cells" which are common in stress-driven, depth-limited turbulent flows [*Papavassiliou and Hanratty*, 1997; *Sullivan et al.*, 2004; *Tejada-Martinez and Grosch*, 2007]. These coherent structures, however, do not appear as organized as the observed ones. With LC the simulated crosswind velocity variations are quantitatively (bands of divergence/convergence regions) and qualitatively (VRMS value, band spacing of about 50 m) similar to the observed crosswind velocity variations (compare black dashed and solid lines in Figure 2 (fifth panel) and Figure 3b with Figure 1). In summary, the simulations agree significantly better with observations if the LC effect is included in the simulations.

[29] It is furthermore insightful to compare our results to previous coastal ocean observations from *Gargett and Wells* [2007]. Consistent with their observations the maximum downward velocity occurs at a depth of about $z = -0.4\ H$ (*Gargett and Wells* [2007] find $z = -0.5\ H$ to $-0.3\ H$). The ratio between crosswind upwelling to downwelling length is about 1.4, i.e., close to the observed values between 1.1 and 1.4 for selective records. Furthermore, as in the observations, simulated variances $\langle u'^2 \rangle$ are close to $\langle v'^2 \rangle$ in the LC case, whereas $\langle u'^2 \rangle \gg \langle v'^2 \rangle$ without LC. Finally, we capture the observed intensification of along-wind velocities close to the bottom below downwelling regions.

## 4. Significance of LC

[30] Based on the LES results, we next contrast the differences between the LC and no LC cases by analyzing the energetics, vertical transport, and Lagrangian particles.

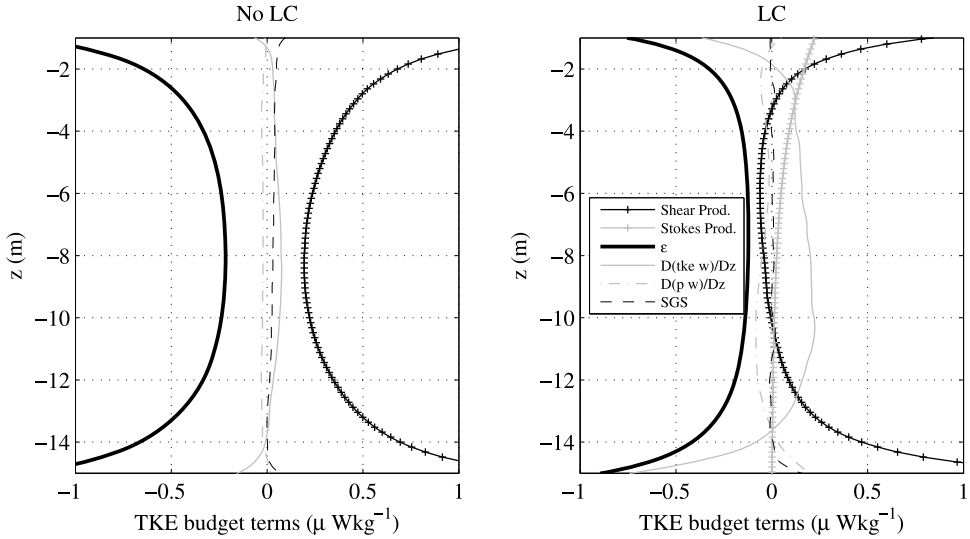


**Figure 4.** Terms of the TKE budget (2).

### 4.1. Horizontally Averaged TKE Budgets

[31] Any dependent variable $q$ is decomposed into horizontal mean $\langle q \rangle$ and its deviation from this mean $q'$, so that

$$q = \langle q \rangle + q'. \tag{1}$$

For the stationary state considered here the turbulent kinetic energy (TKE) balance is [e.g., *McWilliams et al.*, 1997]

$$0 = -\langle u'w' \rangle \frac{\partial u_s}{\partial z} - \langle u_i'w' \rangle \frac{\partial \langle u_i \rangle}{\partial z} - \frac{\partial}{\partial z}\left(\frac{1}{2}\langle u_i'u_i'w' \rangle + \rho^{-1}\langle p'w' \rangle\right) - \epsilon + \mathrm{SGS}, \tag{2}$$

where the terms on the right-hand side are, from left to right, TKE production due to Stokes drift shear, TKE production/distruction due to Eulerian shear, vertical energy flux divergence due to turbulent TKE transport and pressure work, and the TKE dissipation rate $\epsilon$. SGS represents all other unresolved subgrid scale terms (i.e., except for $\epsilon$ [see *Skyllingstad et al.*, 2000]) which are typically less than 5% of the largest resolved TKE budget term (thin dashed line in Figure 4). Note that our TKE budget analysis focuses on the interior flow (away from surface and bottom boundary layers) using a LES where the small-scale turbulence close to the boundaries is modeled rather than resolved. Thus our TKE budget cannot be directly compared to that of *Tejada-Martinez and Grosch* [2007] where surface and bottom viscous sublayers are resolved.

[32] Without LC the dominant TKE balance is between TKE shear production and dissipation (Figure 4, left). Only at middepth is the divergence of vertical TKE transport also important. This is because TKE is advected from energetic regions close to the boundaries (greater TKE production) and deposited at less energetic middepth regions (smaller TKE production).

[33] With LC the TKE budget differs significantly from the one without LC, as the TKE transport term plays an important role throughout the whole water column (Figure 4, right). At depths between approximately 4 and 12 m, the two leading terms in the TKE budget are dissipation and vertical TKE transport. This finding is consistent with the LES results from *Tejada-Martinez et al.* [2012], who show that the log layer of a hydrodynamically smooth flow with its dominant balance between dissipation and production is disrupted in the presence of LC.

[34] Although wave effects significantly modify the TKE budget, the total, i.e., vertically integrated, Stokes drift shear production contributes directly only a small fraction to the total energy input to the system (due to wind and waves). This can be seen by considering the total energy input into the system due to stresses acting on the Stokes drift ($I_s$) and Eulerian currents ($I$)

$$I_s = u_*^2 u_{s0} \quad \text{and} \quad I = u_*^2 \langle u \rangle_0, \tag{3}$$

where $u_*$ is the water friction velocity, $u_{s0}$ is the surface Stokes drift and $\langle u \rangle_0$ is $\langle u \rangle$ at $z = 0$ . Note that $u_*^2 \langle u \rangle_0$ is the energy surface flux due to the surface stress $u_*^2$ acting on the mean surface current $\langle u \rangle_0$. The fraction of energy input of $I_s$ relative to $I$ is

$$\frac{I_s}{I} = \frac{u_{s0}}{\langle u \rangle_0} = \frac{0.014\,\mathrm{m/s}}{0.248\,\mathrm{m/s}} \approx 5\%. \tag{4}$$

This suggests that although the energy input due to Stokes drift shear production is relatively small, the mechanism of stretching and tilting vertical vorticity into the wind direction is an important physical process, significantly redistributing TKE. Furthermore, as one reviewer of this paper pointed out, much of the TKE production is dissipated in the energetic surface and bottom boundary layers and may thus not contribute to the interior mixed layer dynamics. Therefore, the surface Stokes drift and the magnitude of the Eulerian mean surface velocity (related to $u_*$) are generally not sufficient to scale Langmuir turbulence characteristics.

[35] One peculiar feature is the negative TKE production between depths of about 3 m and 10 m, which is due to negative gradients in the mean velocity profile (Figure 5).

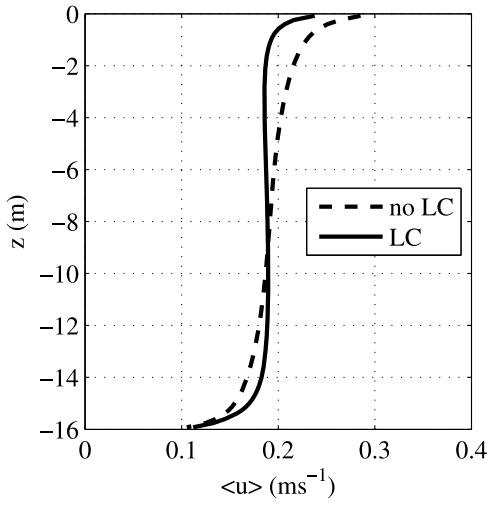


**Figure 5.** Horizontally averaged along-wind velocity profiles $\langle u \rangle$.

Note that both velocity profiles with and without LC resemble qualitatively the respective ones obtained from the simulations of *Tejada-Martinez and Grosch* [2007]. Physically, the negative TKE production can be understood by considering the nonlocal nature of the transport, which is a common, yet insufficiently explored, phenomenon in the presence of relatively large-scale coherent motions. Large-scale coherent motions provide an efficient mechanism to flux relatively high along-wind momentum close to the surface to greater depths roughly between $z = -10$ m and $z = -14$ m. Therefore, one anticipates that the along-wind mean current $\langle u \rangle$ has two peaks, one near the surface and the other somewhere at greater depth where the momentum is deposited (say between $z = -10$ m and $z = -14$ m, Figure 5). As a consequence $\langle u \rangle$ contains a local minimum (between the two peaks), which is for our simulations roughly located at $z = -3$ m with a negative current shear between the local $\langle u \rangle$ minimum and the deeper $\langle u \rangle$ peak. Thus, locally it appears as if turbulence produces mean kinetic energy, since the momentum flux is downward throughout the whole water column. Physically, however, it is important to keep in mind that large-scale, nonlocal LC motion transports momentum away from the boundaries. Also, examination of $\{u\}'$ [see, e.g., *Kukulka et al.*, 2011, Figure 13] reveals that downwind velocity fluctuations are intensified in downwelling regions at the surface and near the bottom, which is consistent with the results of *Tejada-Martinez and Grosch* [2007].

### 4.2. TKE Budget of Dominant LC Scale

[36] The previous discussion prompts the question what maintains LC energetically, in particular given that the energy input due to the Stokes drift shear is only a small fraction of the total energy input to the TKE budget. To investigate this, we derive an energy balance for the coherent motion based on along-wind averages, which exploits the symmetry of the large-scale coherent features

$$\{q\}(t,y,z) = L_x^{-1} \int_0^{L_x} q(t,x,y,z)dx. \tag{5}$$

Thus, any field $q$ can be decomposed into

$$q = \{q\} + q'' = \langle q \rangle + \tilde{q} + q''. \tag{6}$$

Note that by definition $\tilde{q} = \{q\}'$, $\langle \{q\} \rangle = \langle q \rangle$, $q' = \tilde{q} + q''$, and $q''$ is the deviation from the along-wind average ("small-scale incoherent motion" or $u_i''$ motion), and $\tilde{q} = \{q\}'$ is the "large-scale coherent motion" ($\tilde{u}_i$ motion). Note that the same decomposition was employed by *Tejada-Martinez and Grosch* [2007]. Resolved turbulent kinetic energy budgets can be derived for both motions.

[37] The kinetic energy budget of the large-scale coherent motion ($\tilde{u}_i$) is expressed as

$$\begin{aligned} 0 = &-\langle \tilde{u}\tilde{w} \rangle \frac{\partial u_s}{\partial z} - \langle \tilde{u}_i \tilde{w} \rangle \frac{\partial \langle u_i \rangle}{\partial z} + \left\langle u_i'' w'' \frac{\partial \tilde{u}_i}{\partial z} \right\rangle \\ &- \frac{\partial}{\partial z} \left( \frac{1}{2} \langle \tilde{u}_i \tilde{u}_i \tilde{w} \rangle + \langle \tilde{u}_i u_i'' w'' \rangle + \langle \tilde{p}\tilde{w} \rangle \right) \\ &- \epsilon_\sim + \text{SGS}. \end{aligned} \tag{7}$$

The right-hand side terms, from left to right, are tilde TKE production due to Stokes drift shear, tilde TKE production due to Eulerian current shear, TKE conversion from tilde motion to double prime motion, vertical flux divergences of (1) self-advection of tilde kinetic energy, (2) turbulent double prime stresses acting on tilde motion, and (3) tilde energy flux due to pressure work. The last two terms are the tilde TKE dissipation rate and all other subgrid scale terms.

[38] The kinetic energy budget of small-scale incoherent motion $u_i''$ is

$$\begin{aligned} 0 = &-\langle u'' w'' \rangle \frac{\partial u_s}{\partial z} - \langle u_i'' w'' \rangle \frac{\partial \langle u_i \rangle}{\partial z} - \left\langle u_i'' w'' \frac{\partial \tilde{u}_i}{\partial z} \right\rangle \\ &- \frac{\partial}{\partial z} \left( \frac{1}{2} \langle u_i'' u_i'' w'' \rangle + \frac{1}{2} \langle u_i'' u_i'' \tilde{w} \rangle + \langle p'' w'' \rangle \right) \\ &- \epsilon_{''} + \text{SGS}. \end{aligned} \tag{8}$$

The right-hand side terms from left to right are double prime TKE production due to Stokes drift shear, double prime TKE production due to Eulerian current shear, TKE conversion from double prime motion to tilde motion (note opposite sign as in tilde TKE budget), vertical flux divergences of (1) self-advection of double prime TKE, (2) advection of double prime TKE by tilde motion, and (3) double prime TKE flux due to pressure work. The last two terms are the double prime TKE dissipation rate and all other subgrid scale terms, respectively. Note that smaller scales cannot advect larger scales and larger scales do not exert work by turbulent stresses on the smaller-scale motion. The sum of the tilde and double prime budgets results in the full TKE budget described above.

[39] Similar to the study of *Tejada-Martinez and Grosch* [2007], the large-scale coherent motion is relatively small without LC, while it is larger with LC (Figure 6). In the LC case the large-scale coherent tilde motion is the largest contributor to total TKE near the ocean bottom (Figure 6, bottom left) and fluxes 60% to 80% of the total momentum at middepth range between $z = -3$ m and $z = -14$ m (Figure 6, bottom middle). In both cases the sum of the residuals of the partial TKE budgets agree well with the total TKE dissipation rate, which has been directly calculated

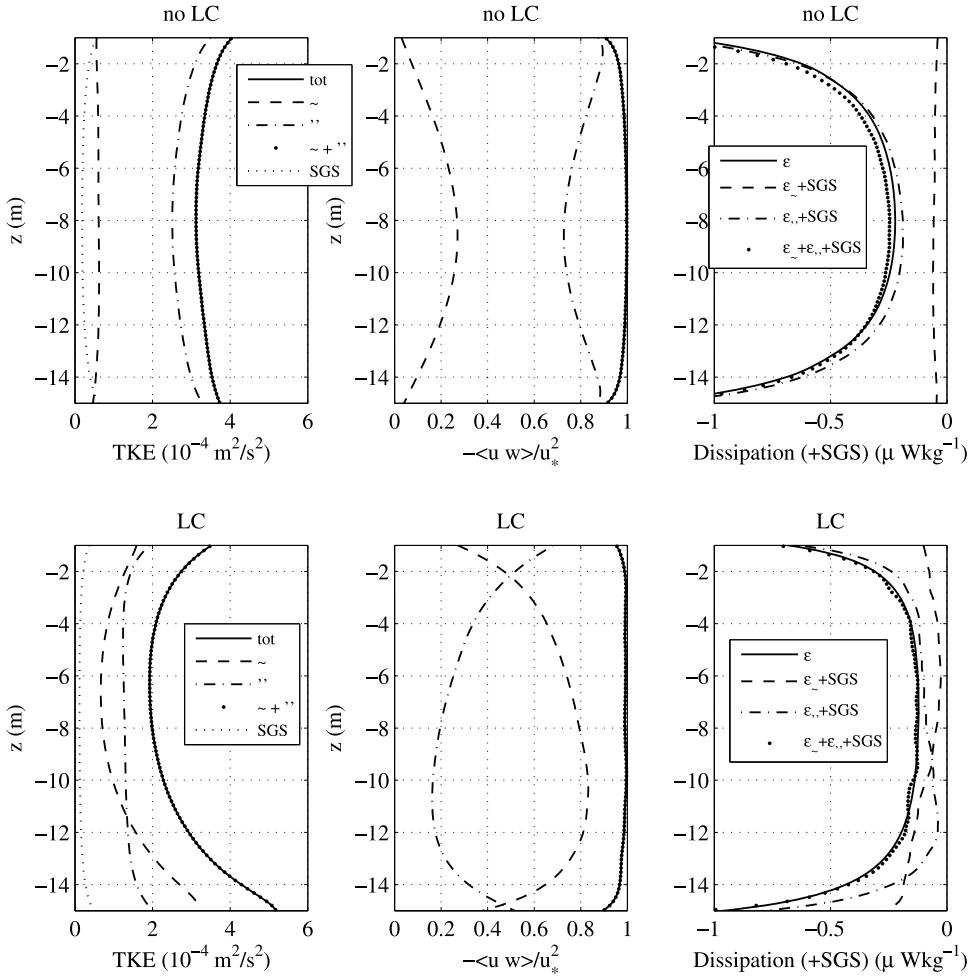


**Figure 6.** (left) Turbulent kinetic energy, (middle) normalized momentum flux, and (right) dissipation rates (top) without and (bottom) with LC due to total motion ($q'$ fields), large-scale coherent motion ($\tilde{q}$ fields), and small-scale incoherent motion ($q''$ fields), as defined in (6).

from the LES model results (Figure 6, right). The close agreement suggests that contributions of SGS terms in the partial budgets are not significant. Note that most of the TKE dissipation is due to incoherent small-scale motion. Because the tilde motion has a larger contribution in the LC simulations, we discuss TKE balances of coherent and incoherent motions only for the LC simulations.

[40] The LC tilde TKE budget is complex (Figure 7, left). The contribution of each budget term, whose significance and sign my change with depth, however, is important. One key result of the tilde TKE budget analysis is that the coherent LC structures extract most of their energy from the Eulerian mean flow rather than from the Stokes drift shear.

[41] The double prime TKE budget is somewhat less complex, as at middepth the dissipation (including SGS contributions) is to first order balanced by double prime TKE advection due to LC motion (Figure 7, right). Near the surface and bottom the dominant balance is between shear production and dissipation. Details of the budget reveal that there are depth ranges where TKE energy production due to Stokes drift shear is significant, which is characteristic of Langmuir turbulence.

### 4.3. Vertical Scalar Transport

[42] In order to examine the vertical scalar transport we consider the evolution of a scalar passive field $S$, whose initial distribution is given by the vertical step function $S(x,y,z \geq -H/2) = 1$ and $S(x,y,z < -H/2) = 0$ (Figures 8 and 9). Without LC the sharp gradient at $z = -H/2$ is gradually smoothed until the horizontally averaged vertical $S$ profile is relatively well mixed after about 40 min (Figure 9, top left). The corresponding resolved turbulent fluxes $-\langle Sw \rangle$ are largest at middepth, where variations in $S$ and $w$ are largest (Figure 9, bottom left). Scalar vertical transport is significantly larger with LC for the first 20 min (by a factor of about 2 for $-4$ m $< z < -12$ m), so that the horizontally averaged $S$ profiles appear to be well mixed 20 min after the tracer release (Figure 9, right). However, rather than being well mixed $S$ remains organized because high $S$ patches are transported in downwelling regions, while low $S$ patches are advected in upwelling regions (see Figure 8 (right) 15 min after development). As a result, the turbulent flux of $S$ changes sign after about 30 min and transports deep high $S$ back upward (Figure 8, right). Note that coherent along-wind vorticies are also present without LC. However, these are

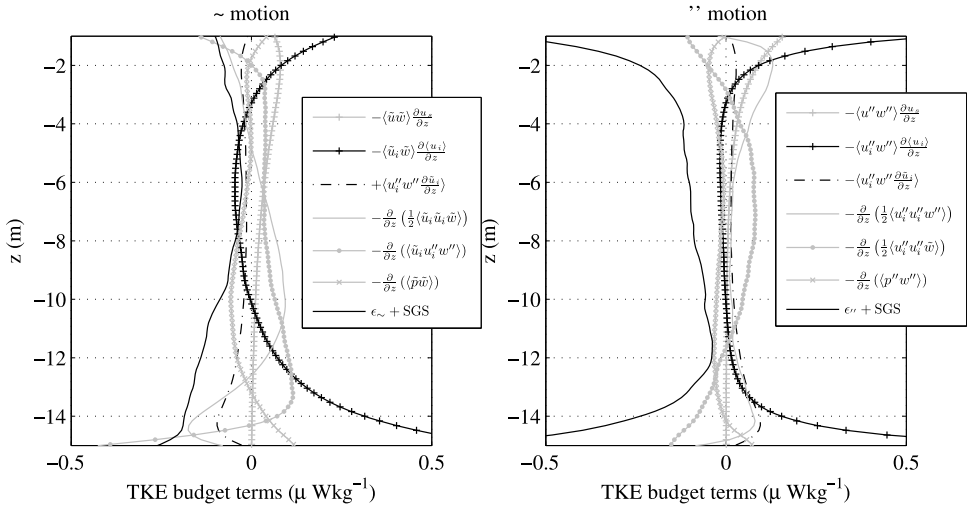


**Figure 7.** TKE budgets (left) of large-scale coherent motion (7) ($\tilde{q}$ fields) and (right) of small-scale incoherent motion (8) ($q''$ fields).

significantly weaker than the ones from the LC case. After 1 h of the tracer release $S$ appears to be more homogenized (mixed) without LC, although the vertical transport is significantly enhanced with LC. Such nonlocal transport due to LC cannot be captured by simple eddy viscosity concepts for horizontally averaged vertical transport.

[43] Because of the nonlocal transport and horizontally inhomogeneous organization of scalar fields the local eddy viscosity concept based on horizontal averages is not physical. In both cases eddy viscosities are very large if the transport is nonzero and vertical gradients vanish. In the LC case the eddy viscosity approaches infinity when profiles appear "well mixed" (in a horizontally averaged sense) and changes sign if $S$ is transported upward the horizontally averaged concentration gradient. Thus, it is challenging to parameterize the net vertical transport because the instantaneous transport depends on the relative positions of the scalar and velocity fields.

[44] The "backward" transport in the LC case is possible because fields remain organized although transport is significant. In particular, LC currents may organize and redistribute fields while potentially suppressing small-scale mixing. Therefore, it is important to distinguish organized advective transport ("stirring") and irreversible small-scale molecular transport ("mixing") [see, e.g., *Müller and Garrett*, 2001]. Small-scale mixing leads to a reduction of the scalar variance. Without boundary fluxes, the volume averaged mean square balance is

$$\frac{d}{dt}\overline{\langle S^2\rangle} = -\overline{\left\langle D\frac{\partial S}{\partial x_i}\frac{\partial S}{\partial x_i}\right\rangle}$$

where $D$ is the molecular diffusion coefficient of $S$ and the over bar indicates depth averages. In the previous equation $S$ is not SGS averaged. In the LES, unresolved subgrid scale fluxes lead to irreversible mixing, so that changes in $\overline{\langle S^2\rangle}$ are not only due to molecular processes but also include SGS stirring processes. The mean square $\overline{\langle S^2\rangle}$ continuously decreases as $S$ transitions from the organized initial state to a less organized mixed state (Figure 10). Once fields are well-mixed $\overline{\langle S^2\rangle}$ approaches a constant minimum value. Interestingly without LC, $S$ homogenizes more quickly, indicating that LC may organize $S$.

[45] The role of turbulence in irreversible mixing is to enhance regions of high gradients so that elevated irreversible molecular exchange takes place. Our results indicate that small-scale turbulence may increase such regions relative to the organized LC motion with relatively weak small-scale motion (see Figure 6). Note also that TKE and associated dissipation rates are larger for the case without wave forcing, as discussed in sections 4.1 and 4.2. Finally, flow structures may enhance or suppress mixing, e.g., the interior of large-scale persistent vorticies may contain kinematical barriers to transport that constrain the motion, alike those often found in ocean gyres [*Wiggins*, 2005]. Investigating in detail potential barriers and teasing apart contributions of stirring and mixing to changes of the scalar variance in a three-dimensional LES flow, where mixing is parameterized, is a complex research task that may require a dynamical systems approach [*Wiggins*, 2005]. To investigate the nonlocal transport further it is natural to take a Lagrangian approach by tracking the evolution of particles distributions.

### 4.4. Lagrangian Particles

[46] Lagrangian particles in LC simulations have been previously tracked in two-dimensional models [*Colbo and Li*, 1999], three-dimensional models on two-dimensional planes [e.g., *McWilliams et al.*, 1997] and in the fully three-dimensional LES space [*Skyllingstad*, 2003; *Harcourt and D'Asaro*, 2010]. We introduce 276480 particles evenly spaced at $t = 0$ s. Initially, the first vertical level is 1 m away from the bottom and the last vertical level is 0.5 m away from the surface with 28 vertical levels in between (0.5 m vertical spacing). Each vertical level contains 96 × 96 particles with a 1 m horizontal spacing. These particles are advected by the resolved time-dependent three-dimensional

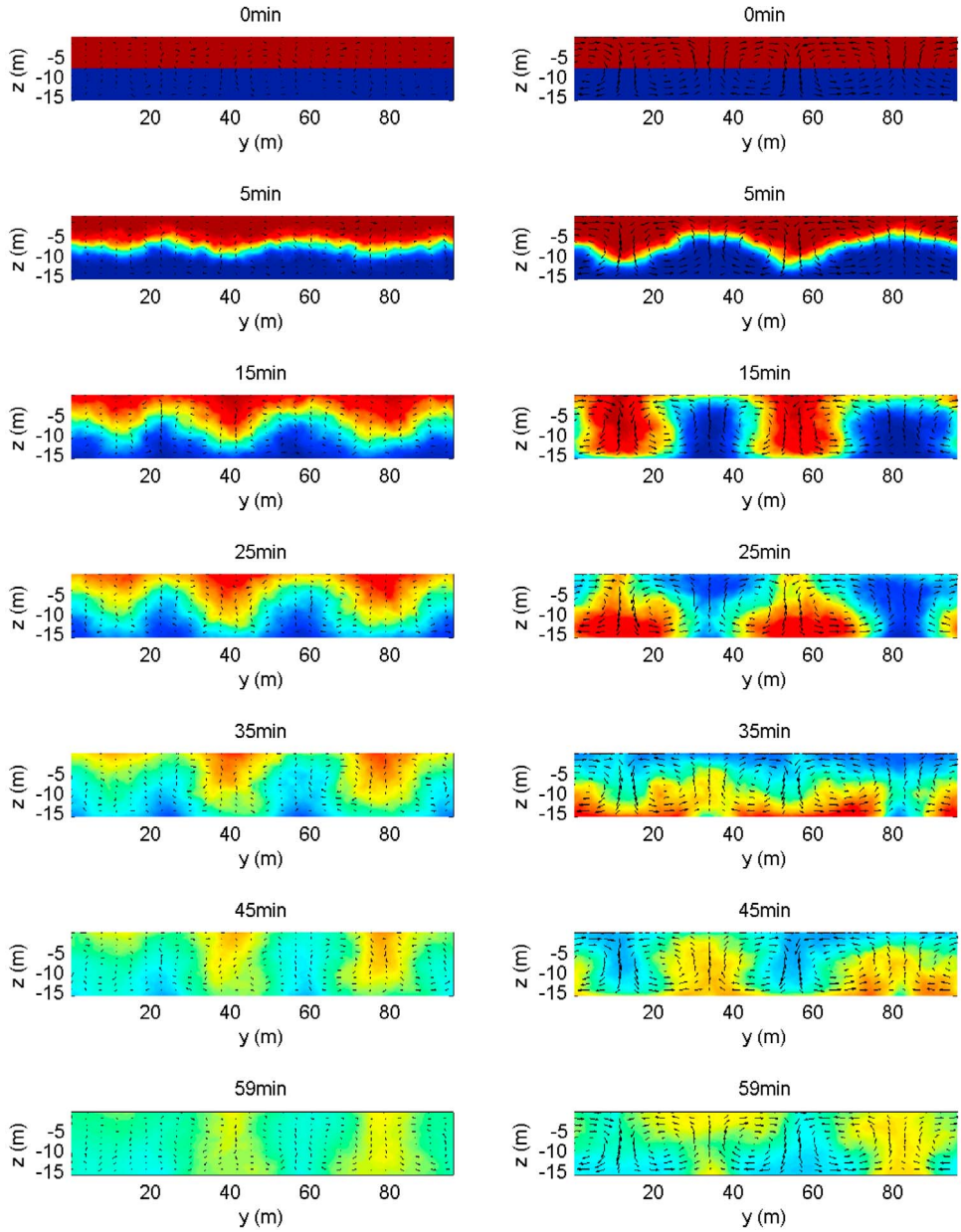


**Figure 8.** Instantaneous along-wind-averaged cross sections of scalar tracer field $S$ (left) without and (right) with LC. Initial tracer distribution is $S = 1$ for the top half of the water column and $S = 0$ for the lower half (same color range as in Figure 9 (top).

flow field, so that we solve for each particle $j$ the ordinary differential equations

$$\frac{dx^j}{dt} = u\left(x^j, y^j, z^j\right) + u_s\left(z^j\right), \tag{9}$$

$$\frac{dy^j}{dt} = v\left(x^j, y^j, z^j\right), \tag{10}$$

$$\frac{dz^j}{dt} = w\left(x^j, y^j, z^j\right), \tag{11}$$

with the initial conditions $\left(x^j, y^j, z^j\right) = \left(x_0^j, y_0^j, z_0^j\right)$ at $t = 0$, as described above. The flow field ($u$, $v$, $w$) is determined from the LES for each time step and linearly interpolated in space. The ordinary differential equations (ODEs) are solved using the same time integration scheme as for the LES (low storage third-order Runge-Kutta method). Our tests and previous studies [e.g., *Gopalakrishnan and Avissar*, 2000] indicate that SGS velocities may be neglected to first order in well-resolved LES studies, although SGS velocities may play a role very close to the boundaries, when they are also, however, the most challenging to model. As a simple test we repeated the scalar mixing experiment with Lagrangian

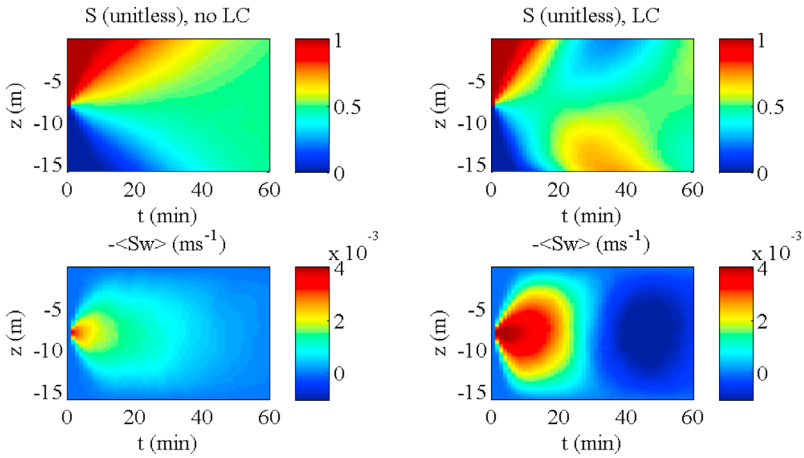


**Figure 9.** (top) Horizontally averaged profile evolution of a passive unitless scalar $S$ and (bottom) associated turbulent vertical transport $-\langle Sw \rangle$. (left) Without LC and (right) with LC.

particles by interpreting $S$ as a particle density distribution and found good agreement between the Eulerian and Lagrangian approaches.

[47] To visualize particle motion we first follow 64 selected particles (from the total of 276,480) in the crosswind-depth plane (Figure 11). With LC, instantaneous particles quickly spread throughout the whole crosswind depth plane, consistent with the relatively large transport. A closer look at the particle trajectories reveals that particles take "preferred paths," as they are either "trapped" in an LC vortex or "sucked" into the adjacent counter rotating vorticies (Figure 11). This provides some insight on why the field $S$ is more organized in the presence of LC.

[48] To understand the vertical dispersion characteristics, we calculate moments of the particle distributions based on the vertical distances of the particles from the origin. The $k$th moment is given by

$$m_z^k(t) = \frac{1}{N}\sum_{j=1}^{N}\left(z^j(t) - z_0^j\right)^k, \qquad (12)$$

so that $m_z^2 = \sigma^2$ is the variance ($\sigma$ the standard deviation), $m_z^3$ is the skewness, and $m_z^4$ is the kurtosis. Because the domain is limited moments approach a constant value for large times

$$m_z^k(\infty) = \int_{-H}^{0} P_0\left(z_0^j\right)\left(\int_{-H}^{0} P_\infty\left(z^j\right)\left(z^j - z_0^j\right)^k dz^j\right) dz_0^j, \qquad (13)$$

where $P_\infty(z)$ is the particle distribution function at $t \rightarrow \infty$ (assumed uniform to compute asymptotes) and $P_0(z)$ is the specified initial particle distribution function. The integral in brackets is the expected value of $\left(z^j - z_0^j\right)^k$ for a particle initially located at $z_0^j$ and the outer integral is the expected value for all initial locations.

[49] Taylor-derived limits of the variance, $\sigma^2$, for times much smaller and much larger than an integral timescale, which is related to $H/u_* \approx 31$ min [*Taylor*, 1922]. For $t \ll H/u_*$, $\sigma^2$ varies approximately as $t^2$ consistent with Taylor's limit (Figure 12, top). Note that $\frac{1}{2}d\sigma^2/dt$ is related to a turbulent diffusivity, which increases nearly linearly initially. For $t \gg H/u_*$, Taylor dispersion limits yield that $\sigma^2$ is proportional to $t$ and $\frac{1}{2}d\sigma^2/dt$ = const. However, in our simulations, particle paths are constrained by the limited vertical domain (the vertical motion is confined between the surface and bottom boundaries), so that all moments approach their asymptotic limit (13) for large times (Figure 12). With LC the maximum turbulent diffusivity is more than twice as large as the one without LC. Note that with LC the variance decreases again, because particles move back toward their initial location. Such a behavior is expected when particles ride in a roll vortex (compare Figure 11).

[50] Without LC values of skewness and kurtosis are initially close to the expected values for Gaussian random velocity, for which $m_z^3 = 0$ (skewness) and $m_z^4/\sigma^4 = 3$ (kurtosis). With LC, the relatively large negative initial skewness is due to downwelling jets, so that particles move more rapidly to greater depths. These large negative values are consistent with relatively narrow downwelling and broader upwelling

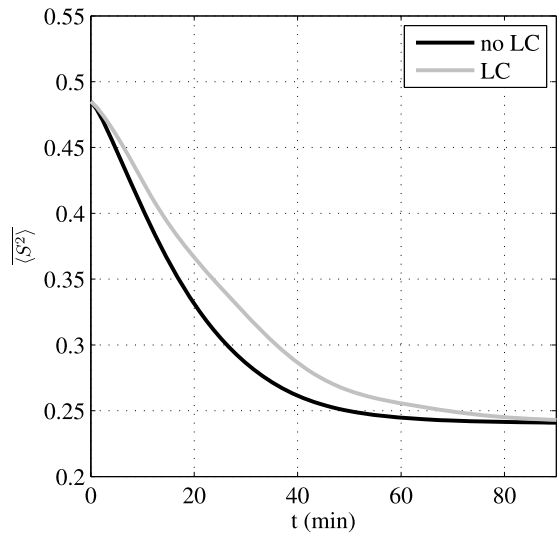


**Figure 10.** Evolution of volume averaged scalar variance $\overline{\langle S^2 \rangle}$ indicates that small-scale mixing is not enhanced in the presence of LC relative to the no LC case, although LC significantly enhances vertical transport.

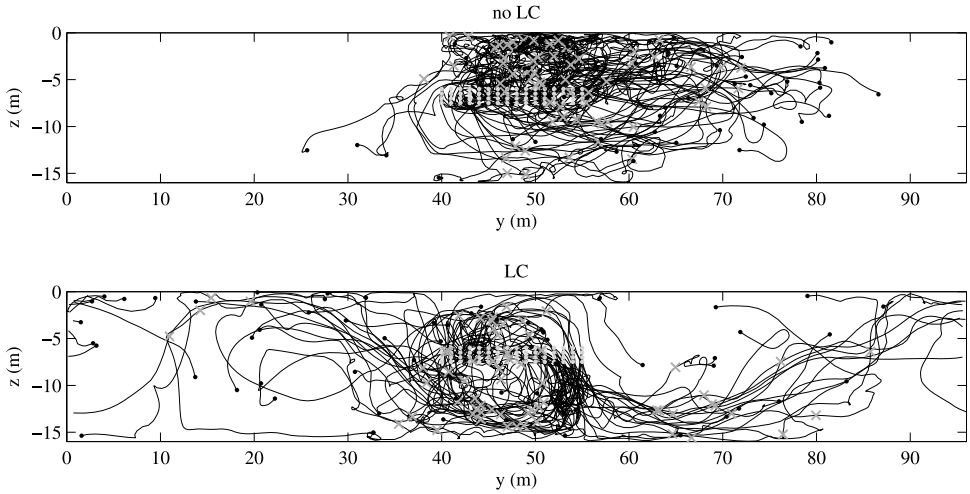


**Figure 11.** Particle trajectories projected into $y/z$ plane of 64 particles initially located at $-8\text{ m} \le z \le -6\text{ m}$ and $40\text{ m} \le y \le 56\text{ m}$ and $x = 88$ m (gray dots); particle positions at $t = 30$ min (crosses) and $t = 60$ min (black dots).

regions. The large kurtosis value reflects that relatively large up and downward velocities occur more often than what would have expected from a Gaussian velocity distribution. Deviations from Gaussian statistics is expected in the presence of coherent features.

[51] Travel of particles throughout the whole water column and associated distributions have potentially important implications for nutrient and light supply of phytoplankton [*Denman and Gargett*, 1995; *Li and Garrett*, 1998]. Phytoplankton critically depends on the nutrient transport from the

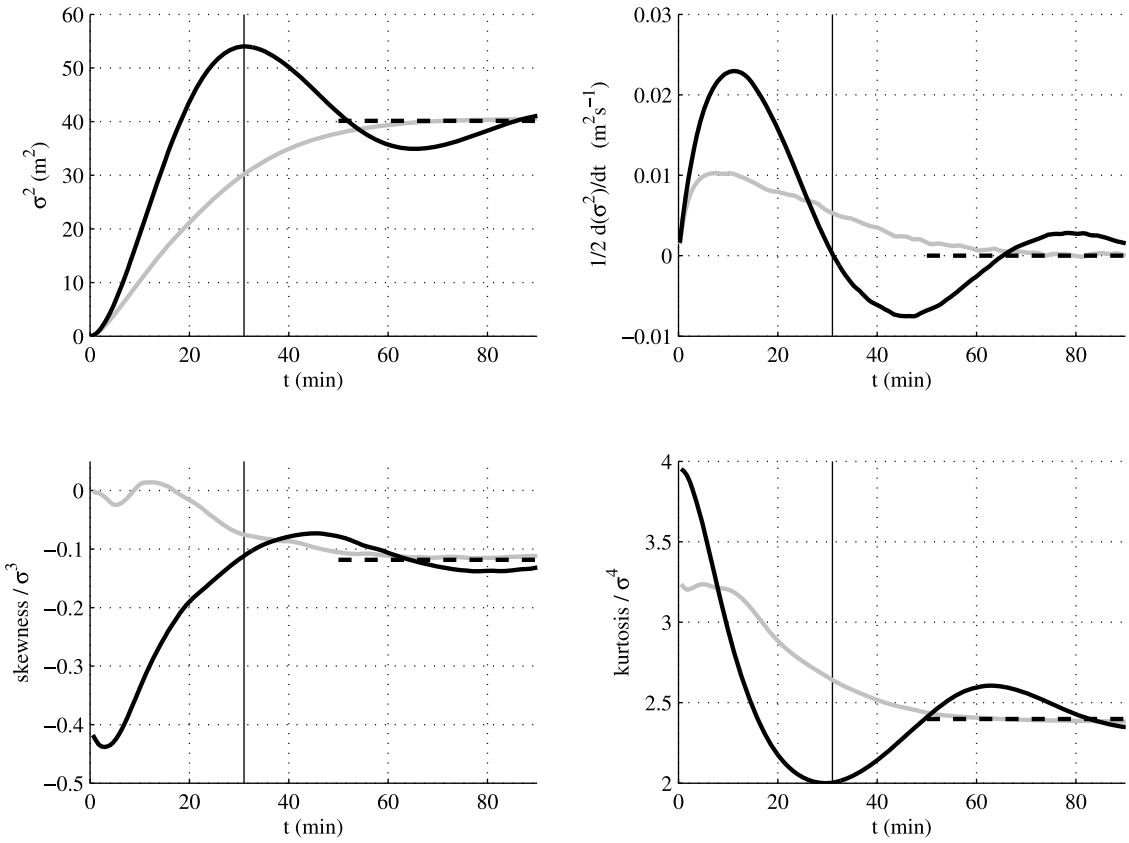


**Figure 12.** Moments of particle distributions based on vertical distances of particles from their initial locations (see (12)), without (gray) and with (black) LC. Dashed line is the asymptotic value for large $t$ (13). An integral timescale is related to $H/u_* \approx 31$ min (black vertical line). Without LC the skewness and kurtosis are closer to what is expected from a Gaussian random velocity field; see main text.

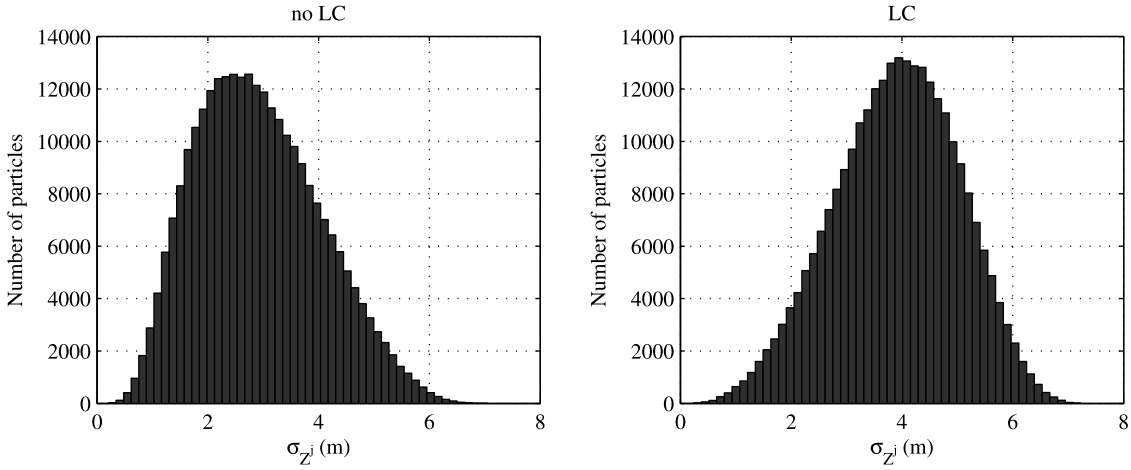


**Figure 13.** The distributions of particle standard deviation $\sigma_z^j$ (see (14)) reveal how far particles travel vertically throughout the whole water column.

bottom to the surface layer. Plankton is also vertically advected in an exponentially decaying light field. Thus, we examine here the typical vertical extent over which a particle travels over a timescale $T = 2\ H/u_*$, and we compute a variance for each particle for the vertical paths

$$\left[\sigma_z^j\right]^2 = \frac{1}{T}\int_0^T \left(z^j - \bar{z}^j\right)^2 dt, \tag{14}$$

where

$$\bar{z}^j = \frac{1}{T}\int_0^T z^j dt. \tag{15}$$

The distributions of standard deviations from each particle is significantly different with and without LC (Figure 13). With LC vertical particle travel distances are significantly larger, allowing particles to approach both the bottom and surface boundary layer. Without LC particles remain much more confined to a certain depth. For example, $\sigma_z^j \geq 4$ m for 48% and 18% of particles with and without LC, respectively.

### 4.5. Buoyant Particles

[52] Strong downwelling and surface convergence regions control the distribution of buoyant material such as, air bubbles, many plankton types, marine plastic debris, or polydisperse oil droplets [*Colbo and Li*, 1999; *D'Asaro*, 2000; *Thorpe*, 2004]. As a first step to illustrate the influence of LC on buoyant material, we introduce a buoyant rise velocity $w_b$ and replace the vertical advection equation by

$$\frac{dz^j}{dt} = w\left(x^j, y^j, z^j\right) + w_b. \tag{16}$$

We set $w_b = 0.5$ cm/s which is consistent with a rise speed of frequently observed dirty air bubbles with a radius of 50 $\mu$m [*Thorpe*, 1982]. We then repeat the particle tracking experiment from section 4.4 (same number of particles, same initial condition). Note that all particles must eventually surface because the SGS motion has been neglected and $w = 0$ at the surface.

[53] Because of the asymmetry of LC upwelling and downwelling regions, buoyant and sinking particles with the same terminal buoyancy speeds will be differently distributed. Buoyant particles will be transported further into the ocean interior.

[54] With LC buoyant particles remain submerged much longer, accumulating in downwelling regions (Figure 14). After 2 h from the initial particle release, 4 times as many particles stay under water and many more particles are found at greater depth. The delayed resurfacing of buoyant particles is qualitatively consistent with earlier ideas of "retention

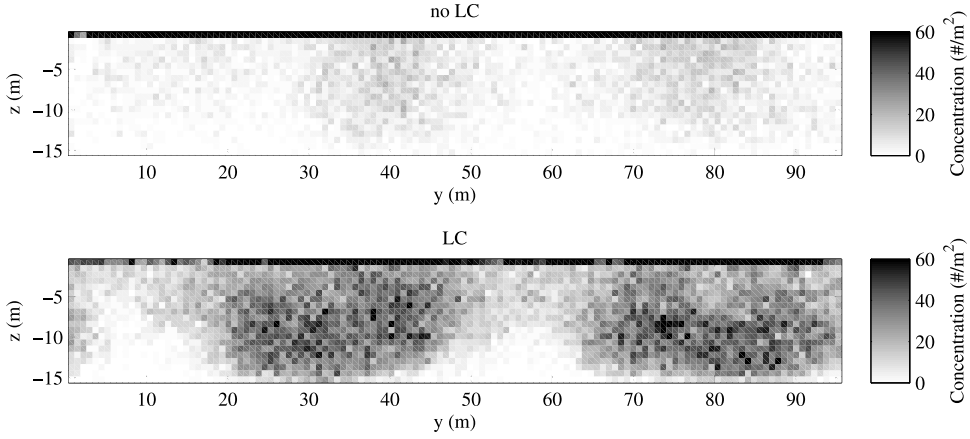


**Figure 14.** Concentration of 276,480 buoyant particles (counts per unit area) in crosswind/depth cross section after $t = 120$ min. With LC significantly more particles remain submerged and organized.

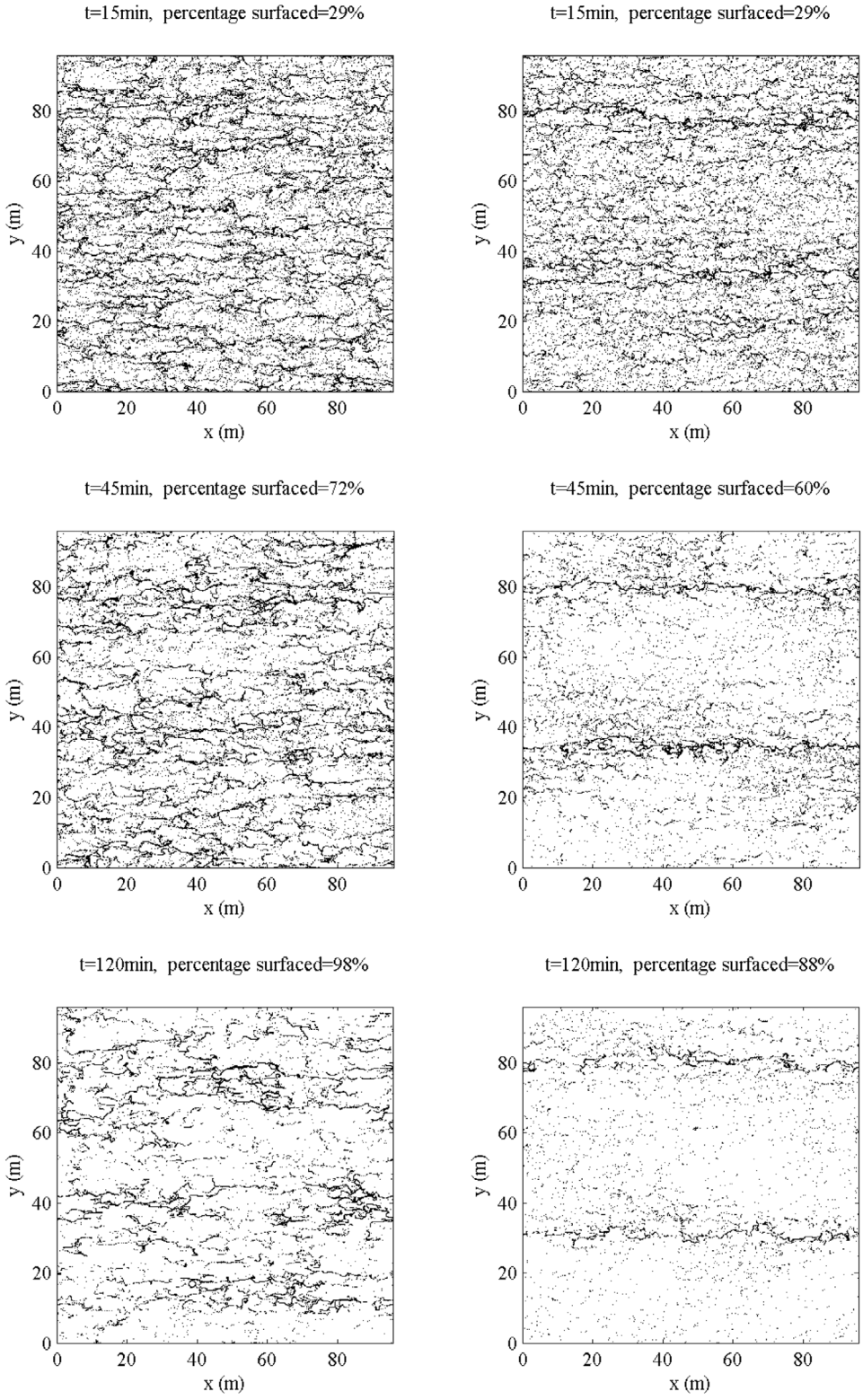


**Figure 15.** (left) Resurfaced particles are trapped in subsurface convergence regions. (right) Locally, much higher particle densities are found in the LC case.

regions" in which particles may be trapped [*Stommel*, 1949]. A quantitative comparison with this model is not appropriate as our cells do not conform to the idealized cell geometry assumed by Stommel and small-scale turbulence transports particles to outside regions. Patches of high particle concentrations form at middepth under LC convergence regions. Surfaced particles are less randomly distributed in the presence of LC and organize quickly in narrow subsurface convergence regions (Figure 15).

This structure agrees with the results from *Skyllingstad* [2003]. Regions of high and low buoyant particle concentrations may strongly influence chemical and biological processes, which depend nonlinearly on material concentrations [e.g., *Fasham et al.*, 1990].

## 5. Conclusions

[55] We analyze observations and simulations of large-scale velocity structures associated with turbulent boundary layer dynamics of a coastal ocean. Special purpose acoustic Doppler current profiler measurements from offshore Massachusetts revealed that such structures persisted for many hours and were frequently present during a 28 day analysis period in October 2003. The presence and strength of these velocity structures is a complex function of environmental conditions, such as tidal currents and nonequilibrium wind seas.

[56] An idealized shallow water large eddy simulation model is designed to capture typical strength and spatial scales of fan beam observations. Simulations are only consistent with the observations if the Langmuir circulation (LC) effect due to wave-current interaction is included in the model. Thus, model results indicate that the observed large-scale velocity structures are due to LC. Based on these simulations, we find that the energetics and transport shift from a local regime for purely shear-driven turbulence to a nonlocal regime for turbulence with LC due to coherent large-scale motions that span the whole water column.

[57] Without LC, turbulent kinetic energy (TKE) dissipation rates approximately balance TKE shear production, consistent with solid wall boundary layer turbulence. This stands in contrast to the LC case for which the vertical TKE transport plays a dominant role in the TKE balance. Surprisingly, the wave term in the TKE balance, converting wave to turbulent energy, is not dominant. Conditional averages indicate that large-scale LC coherent velocity structures extract only a small fraction of energy from the wavefield due to wave-current interaction, but receive most of their energy input from the Eulerian shear TKE production.

[58] The analysis of scalar fields and Lagrangian particles reveals that the vertical transports is significantly enhanced with LC, but that small-scale mixing may be reduced, as a consequence of organized motions. In the presence of LC, vertical scalar fluxes may be along horizontally averaged concentration gradients, violating a common assumption in oceanic boundary layer turbulence parameterizations. Without LC particle statistics are closer to Gaussian statistics than with LC. In particular, particles travel swiftly throughout the whole water column in the presence of LC, encountering highly variable exposure to light intensity and nutrient concentration.

[59] **Acknowledgments.** This work was supported by the U.S. National Science Foundation (Grant OCE-1130678). CBLAST-Low analysis was supported by the Office of Naval Research under grants N00014-03-1-0681 and N00014-06-1-0178 to the Woods Hole Oceanographic Institution. Author T.K. received support from Faculty Startup Funds of the School of Marine Science and Policy, University of Delaware. We appreciate stimulating discussions with John Trowbridge during the early stages of this research. We would like to thank one anonymous reviewer and Ann Gargett and Andres Tejada-Martinez for thoughtful reviews that have clarified the manuscript.

## References

Churchill, J. H., A. J. Plueddemann, and S. M. Faluotico (2006), Extracting wind sea and swell from directional wave spectra derived from a bottom-mounted ADCP, *Tech. Rep. 200613*, 34 pp., Woods Hole Oceanogr. Inst., Woods Hole, Mass.

Colbo, K., and M. Li (1999), Parameterizing particle dispersion in Langmuir circulation, *J. Geophys. Res.*, *104*, 26,059–26,068.

Craig, P. D., and M. L. Banner (1994), Modeling wave-enhanced turbulence in the ocean surface layer, *J. Phys. Oceanogr.*, *24*(12), 2546–2559.

D'Asaro, E. (2000), Simple suggestions for including vertical physics in oil spill models, *Spill Sci. Technol. Bull.*, *6*, 209–211.

Deardorff, J. W. (1973), The use of subgrid transport equations in a three-dimensional model of atmospheric turbulence, *J. Fluids Eng.*, *95*, 429–438.

Denman, K. L., and A. E. Gargett (1995), Biological physical interactions in the upper ocean—the role of vertical and small-scale transport processes, *Annu. Rev. Fluid Mech.*, *27*, 225–255.

Edson, J., et al. (2007), The coupled boundary layers and air-sea transfer experiment in low winds, *Bull. Am. Meteorol. Soc.*, *88*(3), 341–356.

Fasham, M. J. R., H. W. Ducklow, and S. M. McKelvie (1990), A nitrogen-based model of plankton dynamics in the oceanic mixed layer, *J. Mar. Res.*, *48*, 591–639.

Gargett, A. E., and J. R. Wells (2007), Langmuir turbulence in shallow water. Part 1. observations, *J. Fluid Mech.*, *576*, 27–61, doi:10.1017/S0022112006004575.

Gargett, A. E., J. Wells, A. E. Tejada-Martinez, and C. E. Grosch (2004), Langmuir supercells: A mechanism for sediment resuspension and transport in shallow seas, *Science*, *306*, 1925–1928.

Gerbi, G. P., J. H. Trowbridge, J. B. Edson, A. J. Plueddemann, E. A. Terray, and J. J. Fredericks (2008), Measurements of momentum and heat transfer across the air-sea interface, *J. Phys. Oceanogr.*, *38*(5), 1054–1072.

Gerbi, G. P., J. H. Trowbridge, E. A. Terray, A. J. Plueddemann, and T. Kukulka (2009), Observations of turbulence in the ocean surface boundary layer: Energetics and transport, *J. Phys. Oceanogr.*, *39*(5), 1077–1096.

Gnanadesikan, A., and R. Weller (1995), Structure and variability of the Ekman spiral in the presence of surface gravity waves, *J. Phys. Oceanogr.*, *25*, 3148–3171.

Gopalakrishnan, S. G., and R. Avissar (2000), An les study of the impacts of land surface heterogeneity on dispersion in the convective boundary layer, *J. Atmos. Sci.*, *57*, 352–371.

Harcourt, R. R., and E. A. D'Asaro (2008), Large eddy simulation of Langmuir turbulence in pure wind seas, *J. Phys. Oceanogr.*, *38*, 1542–1562.

Harcourt, R. R., and E. A. D'Asaro (2010), Measurement of vertical kinetic energy and vertical velocity skewness in oceanic boundary layers by imperfectly lagrangian floats, *J. Atmos. Oceanic Technol.*, *27*, 1918–1935.

Kukulka, T., A. J. Plueddemann, J. H. Trowbridge, and P. P. Sullivan (2011), The influence of crosswind tidal currents on Langmuir circulation in a shallow ocean, *J. Geophys. Res.*, *116*, C08005, doi:10.1029/2011JC006971.

Leibovich, S. (1977), Convective instability of stably stratified water in the ocean, *J. Fluid Mech.*, *82*, 561–581.

Leibovich, S. (1983), The form and dynamics of Langmuir circulations, *Annu. Rev. Fluid Mech.*, *15*, 391–427.

Lentz, S. J., R. K. Shearman, and A. J. Plueddemann (2010), Heat and salt balances over the New England continental shelf, August 1996 to June 1997, *J. Geophys. Res.*, *115*, C07017, doi:10.1029/2009JC006073.

Li, M., and C. Garrett (1998), Large eddies in the surface mixed layer and their effects on mixing dispersion and biological cycling, in *Physical Processes in Lakes and Oceans*, *Coastal Estuarine Stud.*, vol. 54, edited by J. Imberger, pp. 61–86, AGU, Washington, D. C.

Li, M., C. Garrett, and E. Skyllingstad (2005), A regime diagram for classifying turbulent large eddies in the upper ocean, *Deep Sea Res., Part I*, *52*(2), 259–278.

McWilliams, J. C., P. P. Sullivan, and C. H. Moeng (1997), Langmuir turbulence in the ocean, *J. Fluid Mech.*, *334*, 1–30.

Melville, W. K. (1996), The role of surface-wave breaking in air–sea interaction, *Annu. Rev. Fluid Mech.*, *28*, 279–321.

Müller, P., and C. Garrett (2001), From stirring to mixing in a stratified ocean, *Oceanography*, *15*, 12–19.

Nimmo-Smith, W. A. M., S. A. Thorpe, and A. Graham (1999), Surface effects of bottom-generated turbulence in a shallow tidal sea, *Nature*, *400*, 251–254.

Papavassiliou, D. V., and T. J. Hanratty (1997), Interpretation of large-scale structures observed in a turbulent plane Couette flow, *Intl. J. Heat Fluid Flow*, *18*, 55–69.

Plueddemann, A., J. Smith, D. Farmer, R. Weller, W. Crawford, R. Pinkel, S. Vagle, and A. Gnanadesikan (1996), Structure and variability of Langmuir circulation during the surface waves processes program, *J. Geophys. Res.*, *101*, 3525–3543.

Plueddemann, A., E. A. Terray, and R. Merrewether (2001), Design and performance of a self-contained fan-beam ADCP, *IEEE J. Oceanic Eng.*, *26*, 54–59.

Polton, J. A., and S. E. Belcher (2007), Langmuir turbulence and deeply penetrating jets in an unstratified mixed layer, *J. Geophys. Res.*, *112*, C09020, doi:10.1029/2007JC004205.

Pope, S. B. (2008), *Turbulent Flows*, 5th ed., 771 pp., Cambridge Univ. Press, Cambridge, U. K.

Skyllingstad, E. (2003), The effects of Langmuir circulation on buoyant particles, in *Handbook of Scaling Methods in Aquatic Ecology: Measurement, Analysis, Simulation*, edited by P. G. Strutton and L. Seuront, pp. 445–457, CRC Press, Boca Raton, Fla., doi:10.1201/9780203489550.ch28.

Skyllingstad, E. D., W. D. Smyth, and G. B. Crawford (2000), Resonant wind-driven mixing in the ocean boundary layer, *J. Phys. Oceanogr.*, *30*(8), 1866–1890, doi:10.1175/1520-0485(2000)030<1866:RWDMIT>2.0.CO;2.

Smith, J. A. (1989), Doppler sonar and surface waves: Range and resolution, *J. Atmos. Ocean. Technol.*, *9*, 149–163.

Smith, J. A. (1992), Observed growth of Langmuir circulation, *J. Geophys. Res.*, *97*, 5651–5664.

Stommel, H. (1949), Trajectories of small bodies sinking slowly through convection cells, *J. Mar. Res.*, *8*, 23–29.

Sullivan, P. P., and J. C. McWilliams (2010), Dynamics of winds and currents coupled to surface waves, *Annu. Rev. Fluid Mech.*, *42*, 19–42, doi:10.1146/annurev-fluid-121108-145541.

Sullivan, P. P., J. C. McWilliams, and J. C. Moeng (1994), A sub-grid-scale model for large-eddy simulation of planetary boundary-layer flows, *Boundary Layer Meteorol.*, *71*, 247–276.

Sullivan, P. P., J. C. McWilliams, and W. K. Melville (2004), The oceanic boundary layer driven by wave breaking with stochastic variability, Part 1. Direct numerical simulations, *J. Fluid Mech.*, *507*, 143–174.

Taylor, G. I. (1922), Diffusion by continuous movements, *Proc. London Math. Soc.*, *s2-20*, 196–212, doi:10.1112/plms/s2-20.1.196.

Tejada-Martinez, A. E., and C. E. Grosch (2007), Langmuir turbulence in shallow water. Part 2. Large-eddy simulation, *J. Fluid Mech.*, *576*, 63–108, doi:10.1017/S0022112006004587.

Tejada-Martinez, A. E., C. E. Grosch, N. Sinha, C. Akan, and G. Martinat (2012), Disruption of bottom log-layer in LES of full-depth Langmuir circulation, *J. Fluid Mech.*, *699*, 79–93, doi:10.1017/jfm.2012.84.

Terray, E., M. Donelan, Y. Agrawal, W. Drennan, K. Kahma, A. Williams, P. Hwang, and S. Kitaigorodskii (1996), Estimates of kinetic energy dissipation under breaking waves, *J. Phys. Oceanogr.*, *26*, 792–807.

Thorpe, S. A. (1982), On the clouds of bubbles formed by breaking wind-waves in deep water, and their role in air–sea gas transfer, *Philos. Trans. R. Soc. London, Ser. A*, *304*(1483), 155–210.

Thorpe, S. A. (2000), Langmuir circulation and the dispersion of oil spills in shallow seas, *Spill Sci. Technol. Bull.*, *6*, 213–223.

Thorpe, S. A. (2004), Langmuir circulation, *Annu. Rev. Fluid Mech.*, *36*, 55–79, doi:10.1146/annurev.fluid.36.052203.071431.

Wanninkhof, R., W. E. Asher, D. T. Ho, C. Sweeney, and W. R. McGillis (2009), Advances in quantifying air-sea gas exchange and environmental forcing, *Annu. Rev. Mar. Sci.*, *1*, 213–244, doi:10.1146/annurev.marine.010908.163742.

Wiggins, S. (2005), The dynamical systems approach to Lagrangian transport in oceanic flows, *Annu. Rev. Fluid Mech.*, *37*, 295–328, doi:10.1146/annurev.fluid.37.061903.175815.

Zedel, L., and D. Farmer (1991), Organized structures in subsurface bubble clouds: Langmuir circulation in the open ocean, *J. Geophys. Res.*, *96*, 8889–8900.